Hindawi
International Journal of Aerospace Engineering
Volume 2021, Article ID 6646235, 18 pages
https://doi.org/10.1155/2021/6646235

Research Article

Influence of Design Parameters on Static Bifurcation Behavior of Magnetic Liquid Double Suspension Bearing

Jianhua Zhao[1,2,3] **Xiaochen Wu**[1] **Fang Han**[1] **Xuchao Ma**[1] **Weidong Yan**[1] **Yingna Liang**[4] **Dianrong Gao**[1,2] **and Guojun Du**[2]

[1]*Fluid Power Transmission and Control Laboratory, Yanshan University, Qinhuangdao 066004, China*
[2]*College of Civil Engineering and Mechanics, Yanshan University, Qinhuangdao 066004, China*
[3]*Jiangsu Provincial Key Laboratory of Advanced Manufacture and Process for Marine Mechanical Equipment, Zhenjiang 212003, China*
[4]*Liren College, Yanshan University, Qinhuangdao 066004, China*

Correspondence should be addressed to Jianhua Zhao; zhaojianhua@ysu.edu.cn

Received 28 November 2020; Revised 15 February 2021; Accepted 28 February 2021; Published 26 March 2021

Academic Editor: Angelo Cervone

Magnetic liquid double suspension bearing (MLDSB) includes electromagnetic system and hydrostatic system, and the bearing capacity and stiffness can be greatly improved. It is very suitable for the occasions of medium speed, heavy load, and starting frequently. Due to the mutual coupling and interaction between electromagnetic system and hydrostatic system, the probability and degree of static bifurcation are greatly increased and the operation stability is reduced. And flow of bearing cavity, coil current, oil film thickness, and galvanized layer thickness are the key parameters to ensure operation safe and stable, which has an important influence on the static bifurcation behavior. So this article intends to establish the coupling model of MLDSB to reveal the range of parameter combination in the case of static bifurcation. The influences of different parameter groups on the singularity characteristics, phase trajectory, $x - t$ curves, and suction basin of the single DOF bearing system are analyzed. The result shows that there are nonzero singularities and static bifurcation occurs when $\varepsilon_2 > 0$ or $\delta_2 > 0$. As the flow of bearing cavity, coil current, oil film thickness, and galvanized layer thickness changes in turn, the singularities will convert between stable focus, unstable focus, stable node, and saddle point, and then the stable limit cycle may be generated. The attractiveness of singularity will change greatly with the flow of the bearing cavity and coil current changes slightly in the case of small current or large flow. The minimal change of galvanized layer thickness will lead to the fundamental change of the final stable equilibrium point of the rotor, while the final equilibrium point is slightly affected by the oil film thickness. This study can provide a reference for the supporting stability of MLDSB.

1. Introduction

Hydrostatic bearing is introduced into electromagnetic bearing to form MLDSB, and its supporting form is electromagnetic suspension with hydrostatic pressure auxiliary. It has the advantages of nonmechanical contact, high supporting capacity and stiffness, and operation stability and then the service life can be efficiently improved. So it is suitable for deep-sea exploration, hydropower generation, and other domains, especially medium-low speed, heavy load, and frequent starting occasion [1].

MLDSB is composed of a bracket, a motor, a coupling, a shaft, two journal bearings, an axial bearing, a motor, and a journal motor as shown in Figure 1.

MLDSB can take full advantage of electromagnetic bearing and hydrostatic bearing. On the premise of not affecting the electromagnetic force, the hydrostatic force can be added into the MLDSB to realize real-time double supporting, and its bearing capacity and supporting stiffness are improved greatly [2].

The radial element of MLDSB is composed of step shaft, magnetic sleeve, supporting chamber, magnetic pole, inlet pipe, shell, coil, outlet, and so on as shown in Figures 2 and 3 [3].

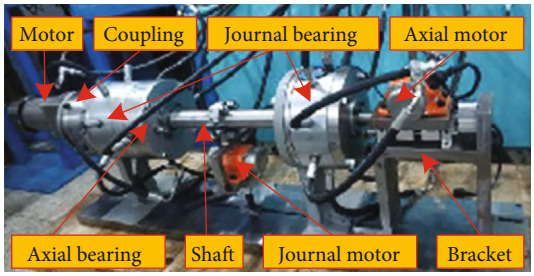

Figure 1: Overall view of MLDSB.

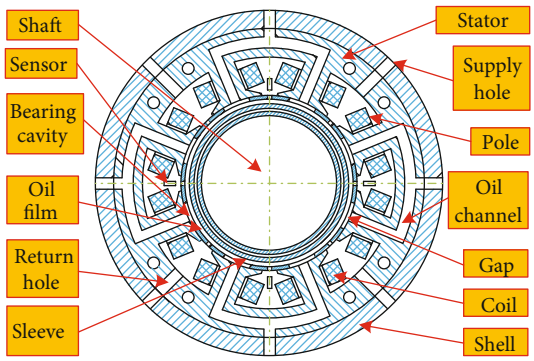

Figure 2: Full profile of radial bearing.

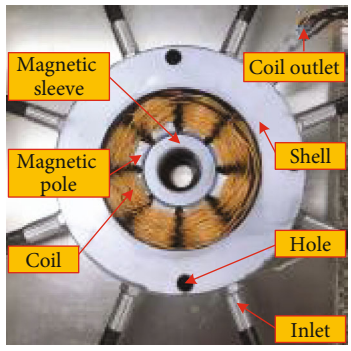

Figure 3: Real products of radial bearing.

The control principle of MLDSB is shown in Figure 4. Constant-flow supply model is adopted in the hydrostatic supporting system, and proportional velocity regulating valves connecting the upper and lower supporting cavities are connected by differential module. PD control is adopted in electromagnetic supporting system, and upper and lower coils are connected through differential connection module. When the rotor is radial offset by external interference, its displacement is adjusted by the hydrostatic supporting system and electromagnetic system, and then it returns to the equilibrium position gradually.

Due to the coupling and interference between the nonlinear electromagnetic system and the nonlinear hydrostatic system, the probability and complexity of static bifurcation are improved, and the reliability and operation stability of MLDSB can be decreased sharply [4]. So many scholars had studied the static bifurcation behavior of electromagnetic suspension bearing and achieved fruitful results.

Wang et al. [5] established the mathematical model of two DOF system under harmonic base motion based on the magnetic force model which can induce bistable phenomena. By the Routh-Hurwitz criterion, the static bifurcation of equilibration points is analyzed for the dimensionless governing equations. The results show that the amplitude-frequency curves of the system are in hard characteristic, while the amplitude variations of the displacement of the piezoelectric cantilever beam with mass ratio and stiffness ratio are in soft characteristic.

Hai and Liu [6] used a unified time-delayed feedback control method to control the spatial static bifurcation of 2-D discrete dynamical systems. The results show that this method can determine and then control the spatial static bifurcation of 2-D discrete dynamical systems by transferring the existing bifurcation or by producing a new fork-shaped, trans-critical, or saddle node bifurcation.

Pu and Hu [7] studied the magneto-elastic principal resonance bifurcation and chaos of rotating annular plates in magnetic fields. The results show that the magnetic field deters the occurrence of multivalue phenomena. With the decreasing of the external force frequency, the rotating speed, and the magnetic induction, and with the increasing of the external force, the system's heteroclinic orbits break more easily, meanwhile, chaos or almost periodic motion of the system is induced.

Luo et al. [8] studied the nonlinear vibration of the rotor system supported by two bearing and excited by electromagnetic force. The results show that the trends of motion of the rotor system in the two displacements are similar. The motions of periodic, pe9 + riod-doubling, and quasiperiodic alternately appear in the operation of the rotor system, and low oil film viscosity is more secure for the rotor system.

Zhao [9] analyzed the nonlinear dynamics phenomenon of cantilever crane. The Lagrange method was used to build the system equation, and the singularity theory was taken to get the bifurcation condition and the normal form of the problem.

Peng [10] established a nonlinear vibration model of parametrically excited stiffness, using the multiple-scale method to solve the amplitude-frequency equation of 1/2 harmonic resonance about the system. The reason that the strip surface appears chatter or vibration marks was found that is caused by the dynamic behaviors such as period, period-3 motion, and chaos of the rolling mill.

To sum up, the current researches only focus on the bifurcation behavior of electromagnetic suspension bearing, while the structure of MLDSB is essentially different from the conventional electromagnetic suspension bearing, and its internal supporting mechanism and behavior law of static bifurcation is more complex. Meanwhile, the design and operation parameters (flow of bearing cavity, coil current, oil film thickness, and galvanized layer thickness) are the premise and foundation of high-performance bearing and stable suspension of MLDSB and have a significant influence on the static bifurcation behavior of MLDSB. So the coupling model of MLDSB is established to explore the internal influence of design and operation parameters on the singularity characteristics, phase trajectory, and suction basin of a single DOF

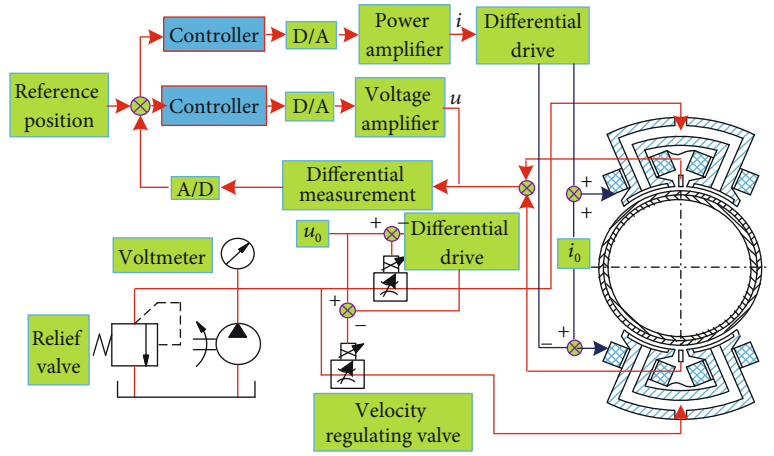

Figure 4: Single DOF support regulation principle of MLDSB.

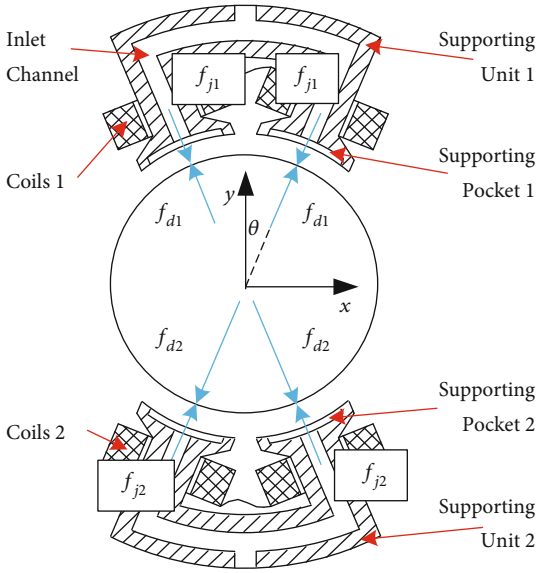

Figure 5: Force diagram of single DOF supporting system.

supporting system, and then the reference can be provided for the design and supporting stability of MLDSB.

2. Bifurcation Range of Design Parameters

Taking the vertical single DOF supporting system as the research object (it includes upper and lower supporting units, rotors, and so on as shown in Figure 5), the dynamic model can be established [11].

$$\begin{cases} \dot{x} = y, \\ \dot{y} = \dfrac{1}{m}\displaystyle\sum_{i=1}^{2} (-1)^{i+1}(F_1 + F_2), \end{cases} \tag{1}$$

where $F_1 = F_{q,0}(y-1)/[1 + (l/h_0) + (-1)^i(x/h_0)\cos\theta]^3$, $F_2 = F_{i,0}[1 + (-1)^{i+1} i_c/i_0/1 + (-1)^i x/h_0 \cos\theta]^2$.

The design parameters of MLDSB are shown in Table 1.

Table 1: Design parameters of MLDSB.

Symbols	Variable names	Sizes
A	Length of supporting cavity	100 mm
B	Width of supporting cavity	20 mm
a	Width of sealing belt	6 mm
b	Width of sealing belt	4 mm
$\bar{B}$	Flow coefficient	4.3611
μ	Dynamic viscosity	1.3077×10^{-3} Pa•s
m	Mass of rotor	100 kg
μ_0	Permeability of air	$4\pi \times 10^{-7}$ H/m
A_e	Area of supporting cavity	1504 mm^2
A_b	Extrusion area	1056 mm^2
A_s	Area of pole	1000 mm^2
θ	Angle	22.5°
N	Number of turns	60
A_1	Area of pole	1000 mm^2
i_0	Initial current	0.5 ~ 2.0A
q	Flow of supporting cavity	$0 \sim 2 \times 10^{-4}$ m^3/s
h_0	Oil film thickness	10~90 μm
l	Galvanized layer thickness	0 ~90 μm
K_p	Proportionality coefficient	-70
K_d	Differential coefficient	0.03

The design and operation parameters include flow q_0 of bearing cavity, coil current i_0, oil film thickness h_0, and galvanized layer thickness l.

2.1. Bifurcation Range of Parameter Group (i_0, q_0). From the definition of bifurcation, it can be seen that the system will not bifurcate when equation (2) has a unique solution, while the system will bifurcate when equation (2) has multiple solutions [12]. The boundary point of static bifurcation can be obtained by solving equations. And then based on the

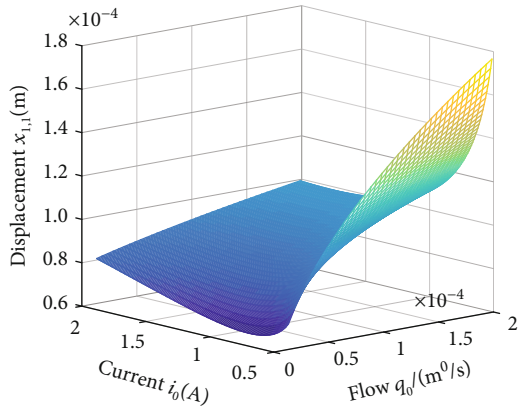

Figure 6: Relationships among $x_{1,1}$, i_0, and q_0.

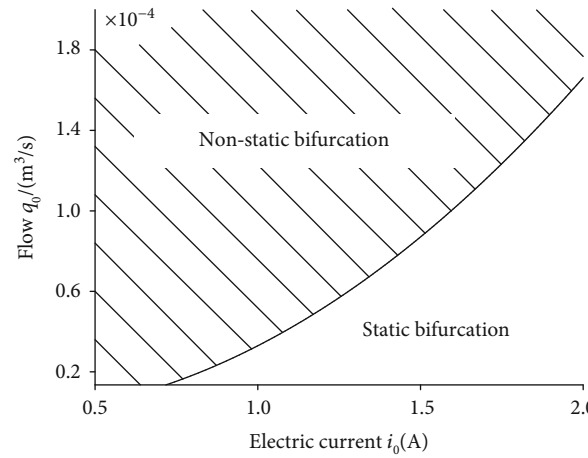

Figure 7: Bifurcation area diagram of electric current and flow.

practical meaning of parameters, the bifurcation range of the system parameters is obtained. Assume that $h_0 = 30\ \mu$m, $l = 0\ \mu$m. According to the definition of singularity, the existence condition of singularity is $\dot{x} = 0$ and $\dot{y} = 0$ [12], then

$$\begin{cases} y = 0, \\ -\dfrac{1}{m}\displaystyle\sum_{i=0}^{1}(-1)^i(F_1 + F_2) = 0. \end{cases} \tag{2}$$

The design parameters in Table 1 were substituted into equation (2), and the coordinates of the singularities were obtained as follows:

$$\begin{cases} (x_0, y_0) = (0, 0), \\ (x_{1,1}, y_1) = (\sqrt{\varepsilon_1}, 0), \\ (x_{1,2}, y_1) = (-\sqrt{\varepsilon_1}, 0), \\ (x_{2,1}, y_2) = (\sqrt{\varepsilon_2}, 0), \\ (x_{2,,2}, y_2) = (-\sqrt{\varepsilon_2}, 0), \end{cases} \tag{3}$$

where, $\varepsilon_i = 5.2697 \times 10^{-28}/184 i_0 - 63(\alpha + (-1)^{i-1}\sqrt{\beta}), i = 1, 2$

$$\begin{aligned} \alpha &= 3.6052 \times 10^{24} q_0 + 5.4219 \times 10^{20} i_0^2 - 6.3562 \times 10^{19}, \\ \beta &= 2.9397 \times 10^{41} i_0^4 - 4.0261 \times 10^{41} i_0^3 + 3.9094 \times 10^{45} i_0^2 q_0 \\ &\quad + 2.0677 \times 10^{41} i_0^2 + 8.0312 \times 10^{45} i_0 q_0 - 4.7198 \times 10^{40} i_0 \\ &\quad - 3.2081 \times 10^{45} q_0 + 4.0401 \times 10^{39} + 1.2997 \times 10^{49} q_0^2. \end{aligned} \tag{4}$$

From equation (3), it can be seen that there is a zero singularity (0, 0) and four nonzero singularities $(x_{1,1}, 0)$, $(x_{1,2}, 0)$, $(x_{2,1}, 0)$, and $(x_{2,2}, 0)$ in MLDSB system.

The relationships among $x_{1,1}$, q_0, and i_0 are shown in Figure 6, and $x_{1,1} = -x_{1,2}$. The displacement $x_{1,1}$ and $x_{1,2}$ are beyond the actual thickness range of the oil film, so the singularities $(x_{1,1}, 0)$ and $(x_{1,2}, 0)$ can be ignored without practical meaning [13].

According to equation (3), static bifurcation occurs and singularity $(x_{2,1}, 0)$ and $(x_{2,2}, 0)$ exists when $\varepsilon_2 > 0$, and then the range of parameter combinations is shown in Figure 7.

2.2. Bifurcation Range of Parameter Group (h_0, l). Similarly, assume that $i_0 = 1.2$ A, $q_0 = 5.4370 \times 10^{-8}$ m^3/s. The parameters in Table 1 are substituted into equation (2) to obtain the singularities as follows.

$$\begin{cases} (x_0, y_0) = (0, 0), \\ (x_{1,1}, y_1) = \left(\sqrt{\delta_1}, 0\right), \\ (x_{1,2}, y_1) = \left(-\sqrt{\delta_1}, 0\right), \\ (x_{2,1}, y_2) = \left(\sqrt{\delta_2}, 0\right), \\ (x_{2,2}, y_2) = \left(-\sqrt{\delta_2}, 0\right), \end{cases} \tag{5}$$

where $\delta_i = -0.5 h_0^2 (h_0 + l)^2/\gamma_2[\alpha_7 + (-1)^{i+1} 1.33 \times 10^{36} \sqrt{\beta_3}], i = 1, 2$

$$\begin{aligned} \alpha_7 &= 4.67 \times 10^{27} h_0 l^4 + 4.67 \times 10^{27} h_0^4 l + 9.34 \times 10^{26} h_0^5 \\ &\quad + 9.34 \times 10^{26} h_0^2 l^3 + 9.34 \times 10^{26} h_0^3 l^2, \\ \beta_2 &= -9.01 \times 10^{-17} h_0^7 l^3 - 1.56 \times 10^{-16} h_0^6 l^4 - 1.89 \times 10^{-16} h_0^5 l^5 \\ &\quad - 1.58 \times 10^{-16} h_0^4 l^6 - 9.01 \times 10^{-17} h_0^3 l^7, \\ \gamma_2 &= 1.16 \times 10^{28} h_0^6 l + 3.49 \times 10^{28} h_0^5 l^2 + 5.81 \times 10^{28} h_0^4 l^3 \\ &\quad + 5.81 \times 10^{28} h_0^3 l^4 + 3.49 \times 10^{28} h_0^2 l^5 + 1.16 \times 10^{28} h_0 l^6. \end{aligned} \tag{6}$$

Similarly, from equation (5), it can be seen that there are only three meaningful singularities (0, 0), $(x_{2,1}, 0)$, and $(x_{2,2}, 0)$, static bifurcation occurs and singularity $(x_{2,1}, 0)$ and $(x_{2,2}, 0)$ exists when $\varepsilon_2 > 0$, and then the range of parameter combinations is shown in Figure 8.

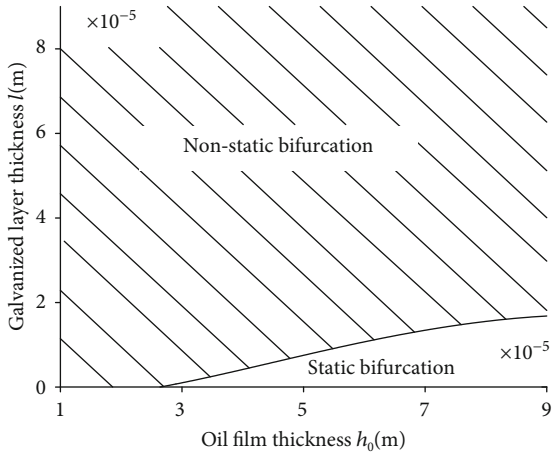

Figure 8: Bifurcation scope diagram.

3. Singularity Characteristics of Single DOF Supporting System

3.1. Singular Points Characteristic under Parameter Groups (i_0, q_0). Equation (1) was rewritten in the following form.

$$\begin{cases} P(x,y) = y, \\ Q(x,y) = -\dfrac{1}{m}\displaystyle\sum_{i=0}^{1}(-1)^i(F_1 + F_2). \end{cases} \tag{7}$$

Jacobian matrix $\boldsymbol{A}$ of x and y can be obtained from equation (7).

$$\mathbf{A} = \begin{pmatrix} \dfrac{\partial P}{\partial x} & \dfrac{\partial P}{\partial y} \\ \dfrac{\partial Q}{\partial x} & \dfrac{\partial Q}{\partial y} \end{pmatrix} = \begin{pmatrix} 0 & 1 \\ \dfrac{\partial Q}{\partial x} & \dfrac{\partial Q}{\partial y} \end{pmatrix}. \tag{8}$$

The characteristic equation of matrix $\boldsymbol{A}$ [14] can be expanded as follows:

$$|\mathbf{A} - \lambda\mathbf{E}| = \lambda^2 - p\lambda + q = 0, \tag{9}$$

where $p = \partial Q/\partial y$, $q = -\partial Q/\partial x$.

3.1.1. Characteristics of Zero Singularity. The singularity (0, 0) was substituted into equation (9) to obtain as follows.

$$\begin{cases} p = 415.99i_0 - 597.17, \\ q = -2.8349 \times 10^6 i_0^2 + 970644i_0 + 5.655 \times 10^{10} q_0, \\ \Delta = p^2 - 4q. \end{cases} \tag{10}$$

According to equation (10), the changing curves of p, q, and $\triangle$ can be obtained as shown in Figure 9 (q coincides with $\triangle$ to form a curve).

According to Figure 9, the coordinate system is divided into four regions:

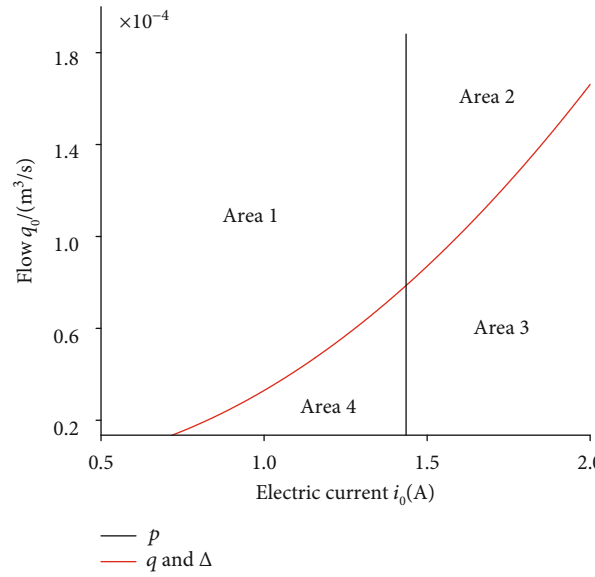

Figure 9: Positive and negative boundary of p, q, and $\triangle$.

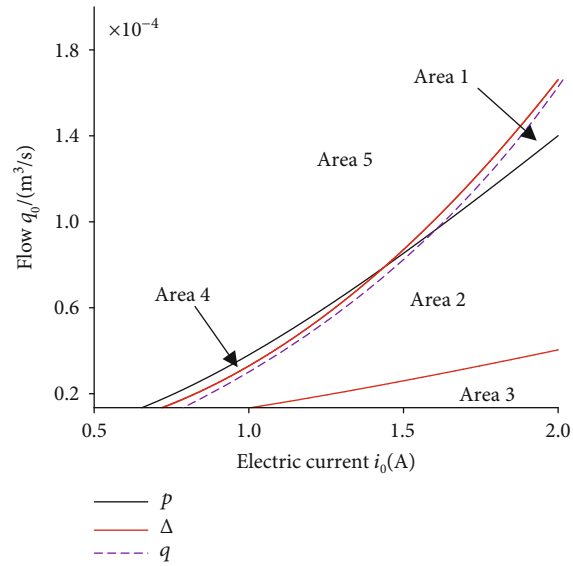

Figure 10: Positive and negative boundary of p, q, and $\triangle$.

(1) In area 1, $p < 0$, $q < 0$, $\triangle < 0$, and the singularities are stable focus

(2) In area 2, $p > 0$, $q > 0$, $\triangle < 0$, and the singularities are unstable focus

(3) In area 3, $p > 0$, $q < 0$, $\triangle > 0$, and the singularities are saddle points

(4) In area 4, $p < 0$, $q < 0$, $\triangle > 0$, and the singularities are saddle points

3.1.2. Characteristics of Nonzero Singularities. Similarly, singularity $(x_2, 0)$ was substituted into equation (9) to obtain curves of p, q, and $\triangle$ as shown in Figure 10.

According to Figure 10, the coordinate system is divided into five regions (the curve q is similar to a part of the curve $\triangle$, the above two can be approximately regarded as a curve).

(1) In area 1, $p > 0$, $q > 0$, $\triangle < 0$, and the singularities are unstable focus

(2) In area 2, $p < 0$, $q > 0$, $\triangle < 0$, and the singularities are stable focus

(3) In area 3, $p < 0$, $q > 0$, $\triangle > 0$, and the singularities are stable focus

(4) In area 4, nonzero singularities are not existing

(5) In area 5, nonzero singularities are not existing

3.2. Singularity Characteristics under Parameter Group (h_0, l). Similarly, the singularity characteristics under the parameter group (h_0, l) are analyzed.

3.2.1. Characteristics of Zero Singularity. Singularity $(0, 0)$ was substituted into equation (9) to obtain p, q, and $\triangle$ as follows:

$$\begin{cases} p = \dfrac{4.49 \times 10^{-7}}{(h_0 + l)^2} - \dfrac{1.61 \times 10^{-11}}{h_0^3}, \\ q = \dfrac{5.99 \times 10^{-4}}{(h_0 + l)^2} - \dfrac{1.10 \times 10^{-7}}{(h_0 + l)^3} + \dfrac{2.49 \times 10^{-12}}{h_0^4}, \\ \Delta = p^2 - 4q. \end{cases} \tag{11}$$

According to equation (11), the curves of p, q, and $\triangle$ can be obtained as shown as Figure 11 (q coincides with $\triangle$ to form a curve).

According to Figure 11, the coordinate system is divided into four regions:

(1) In area 1, $p < 0$, $q > 0$, $\triangle < 0$, and the singularities are stable focus

(2) In area 2, $p > 0$, $q > 0$, $\triangle < 0$, and the singularities are unstable focus

(3) In area 3, $p > 0$, $q < 0$, $\triangle > 0$, and the singularities are saddle points

(4) In area 4, $p < 0$, $q < 0$, $\triangle > 0$, and the singularities are saddle points

3.2.2. Characteristics of Nonzero Singularities. The singularity $(x_2, 0)$ was substituted into equation (9) to obtain the curves of p, q, and $\triangle$ as shown in Figure 12.

As can be seen from Figure 12, the coordinate system is divided into four areas:

(1) In area 1, the singularities are not existing

(2) In area 2, $p > 0$, $q > 0$, $\triangle < 0$, and the singularities are unstable focus

(3) In area 3, $p < 0$, $q > 0$, $\triangle < 0$, and the singularities are stable focus

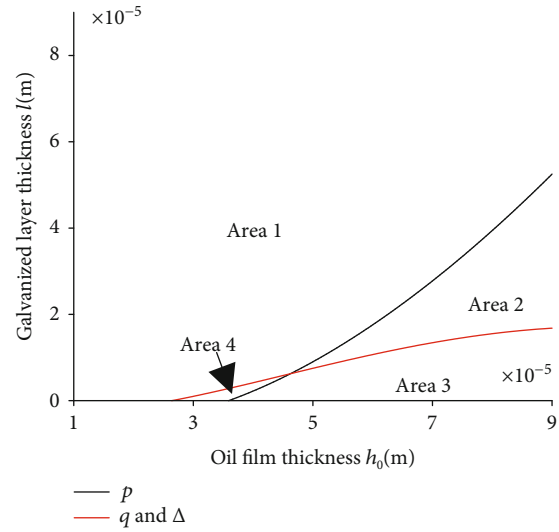

Figure 11: Positive and negative boundary of p, q, and $\triangle$.

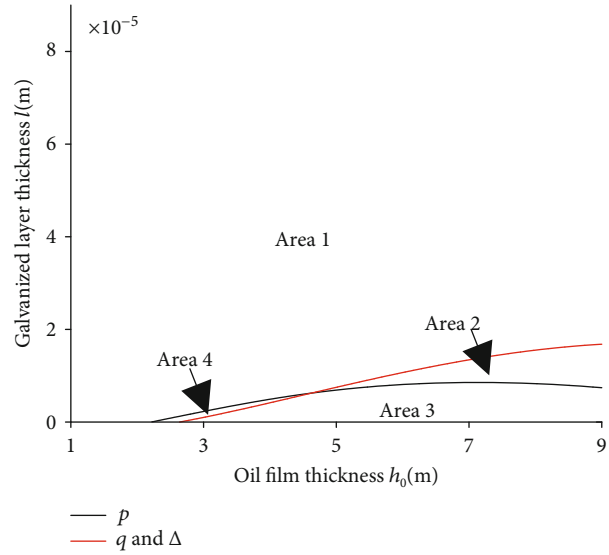

Figure 12: Positive and negative boundary of p, q, and $\triangle$.

(4) In area 4, the singularities are not existing

4. Phase Trajectories and Attractivity of Single DOF Supporting System

4.1. Phase Trajectories and Attractivity under Parameter Groups (i_0, q_0)

(1) Assume that $i_0 = 1.0$ A, $q_0 = 0.3 \times 10^{-4}$ m^3/s, phase trajectories, and $x - t$ curves can be obtained by fourth-order Runge-Kutta method [15] as shown in Figures 13 and 14

The phase trajectories of initial point $(1.5 \times 10^{-5}, -0.02)$ and $(1.5 \times 10^{-5}, 0.02)$, respectively, surround and approach stable focuses $(0.76 \times 10^{-5}, 0)$ and $(-0.76 \times 10^{-5}, 0)$. Both of them reach balance after 0.03 s adjustment, and the rotor

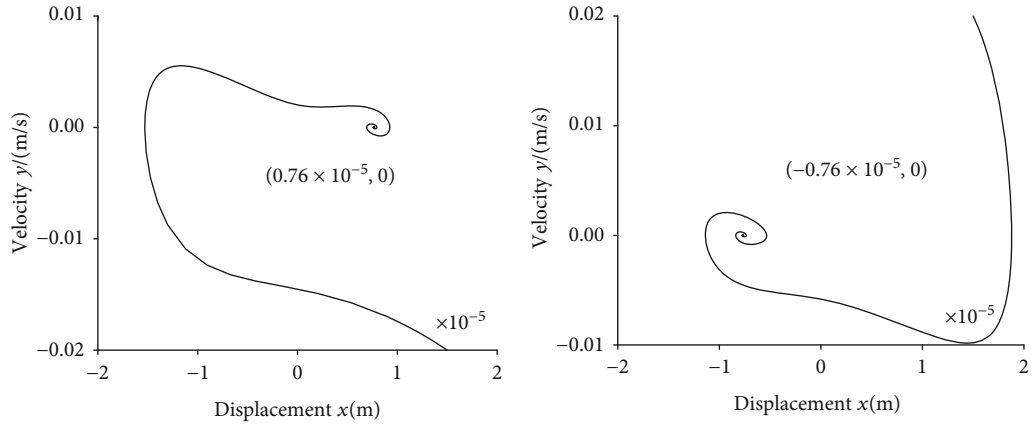

(a) $(x_0 = 1.5 \times 10^{-5}, v_0 = -0.02)$ (b) $(x_0 = 1.5 \times 10^{-5}, v_0 = 0.02)$

FIGURE 13: Phase trajectories under $i_0 = 1.0$ A, $q_0 = 0.3 \times 10^{-4}$ m^3/s.

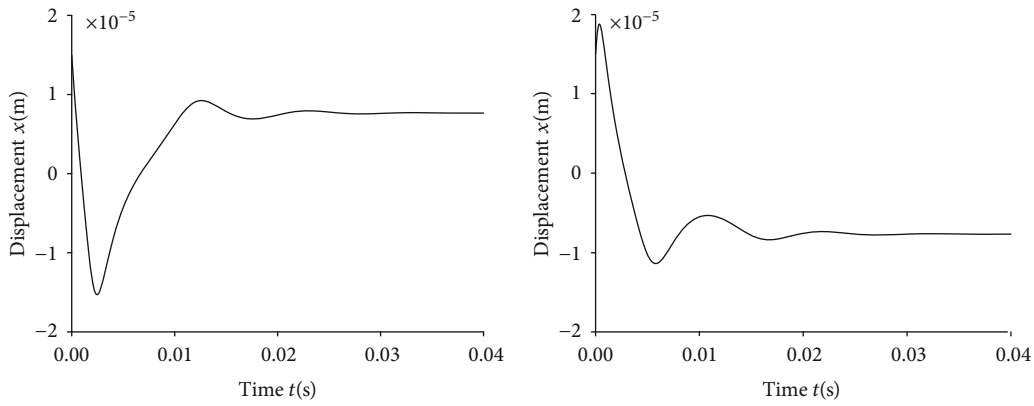

(a) $(x_0 = 1.5 \times 10^{-5}, v_0 = -0.02)$ (b) $(x_0 = 1.5 \times 10^{-5}, v_0 = 0.02)$

FIGURE 14: $x - t$ curves under $i_0 = 1.0$ A, $q_0 = 0.3 \times 10^{-4}$ m^3/s.

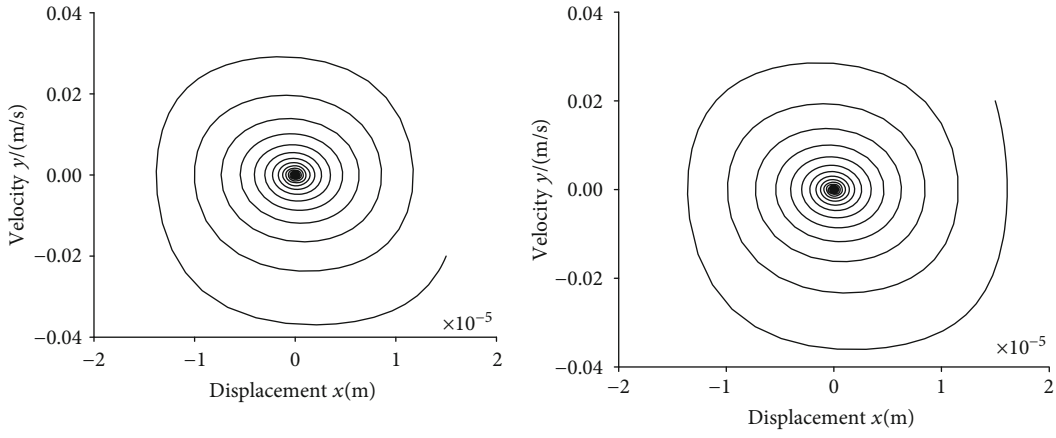

(a) $(x_0 = 1.5 \times 10^{-5}, v_0 = -0.02)$ (b) $(x_0 = 1.5 \times 10^{-5}, v_0 = 0.02)$

FIGURE 15: Phase trajectories under $i_0 = 1.0$ A, $q_0 = 1 \times 10^{-4}$ m^3/s.

can be suspended stably as shown in Figures 13 and 14. However, the balance position is not the expected center of rotation [16].

(2) Assume that $i_0 = 1.0$ A, $q_0 = 1 \times 10^{-4}$ m^3/s, and the phase trajectories and $x - t$ curves [17] are shown in Figures 15 and 16

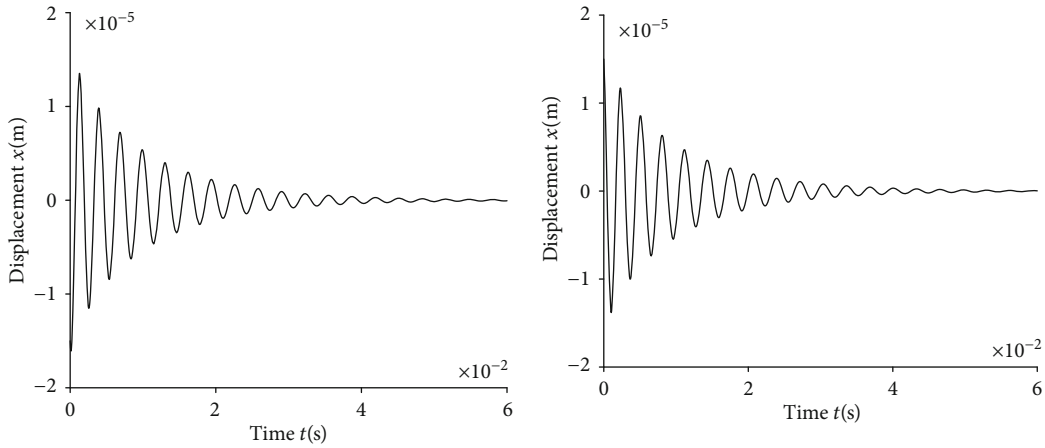

(a) ($x_0 = 1.5 \times 10^{-5}$, $v_0 = -0.02$) (b) ($x_0 = 1.5 \times 10^{-5}$, $v_0 = 0.02$)

FIGURE 16: $x - t$ curves under $i_0 = 1.0$ A, $q_0 = 1 \times 10^{-4}$ m^3/s.

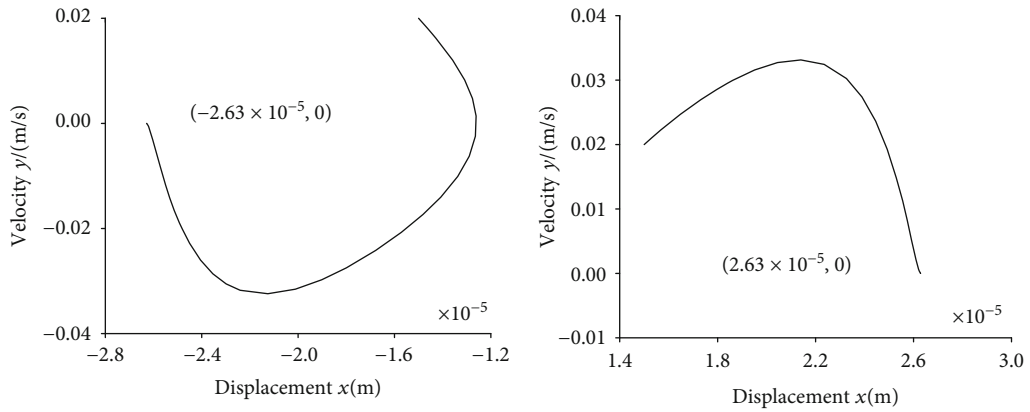

(a) ($x_0 = -1.5 \times 10^{-5}$, $v_0 = 0.02$) (b) ($x_0 = 1.5 \times 10^{-5}$, $v_0 = 0.02$)

FIGURE 17: Phase trajectories under $i_0 = 1.6$ A, $q_0 = 0.25 \times 10^{-4}$ m^3/s.

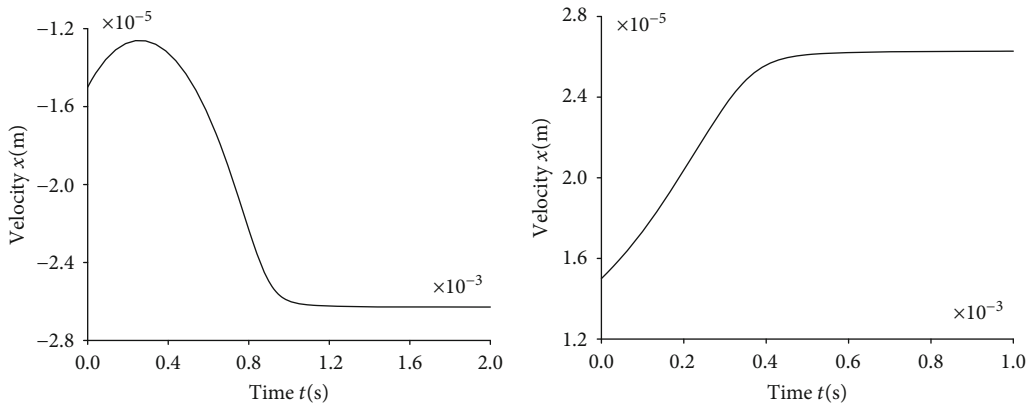

(a) ($x_0 = -1.5 \times 10^{-5}$, $v_0 = 0.02$) (b) ($x_0 = 1.5 \times 10^{-5}$, $v_0 = 0.02$)

FIGURE 18: $x - t$ curves under $i_0 = 1.6$ A, $q_0 = 0.25 \times 10^{-4}$ m^3/s.

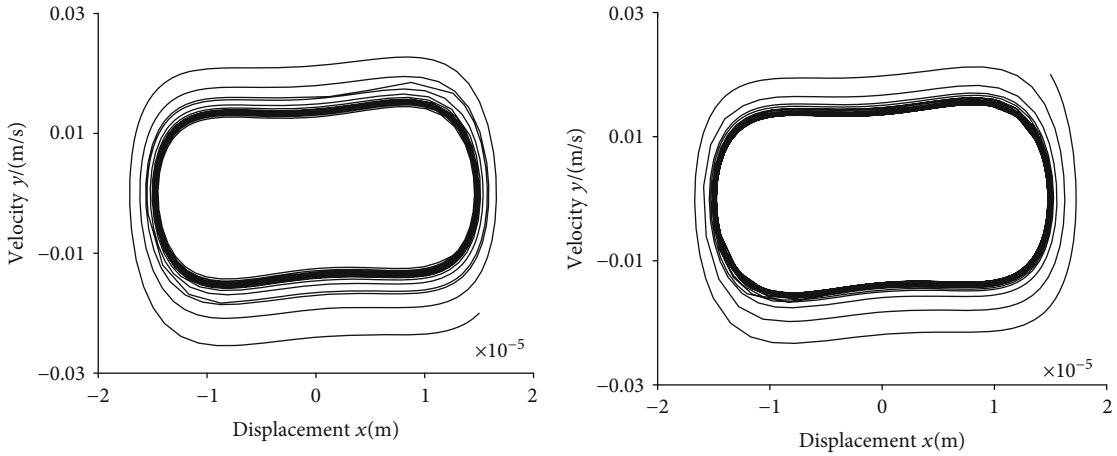

(a) ($x_0 = 1.5 \times 10^{-5}$, $v_0 = -0.02$) (b) ($x_0 = 1.5 \times 10^{-5}$, $v_0 = 0.02$)

Figure 19: Phase trajectories under $i_0 = 1.8$ A, $q_0 = 1.2 \times 10^{-4}$ m^3/s.

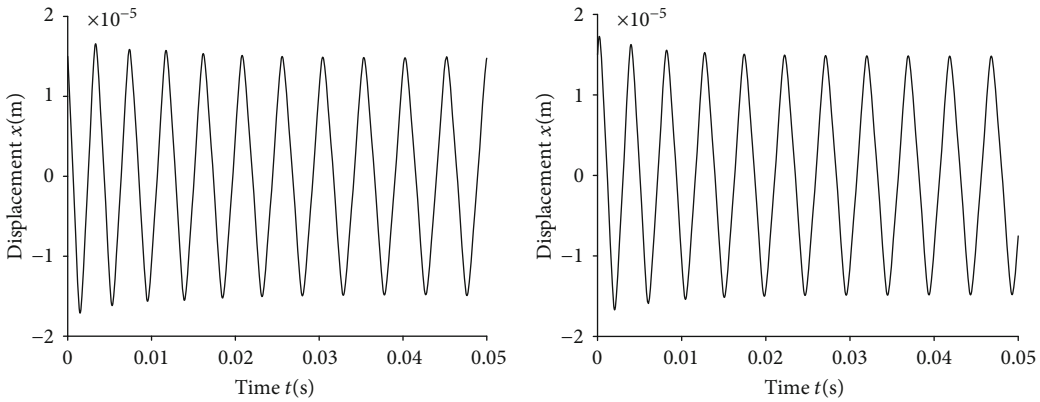

(a) ($x_0 = 1.5 \times 10^{-5}$, $v_0 = -0.02$) (b) ($x_0 = 1.5 \times 10^{-5}$, $v_0 = 0.02$)

Figure 20: $x - t$ curves under $i_0 = 1.8$ A, $q_0 = 1.2 \times 10^{-4}$ m^3/s.

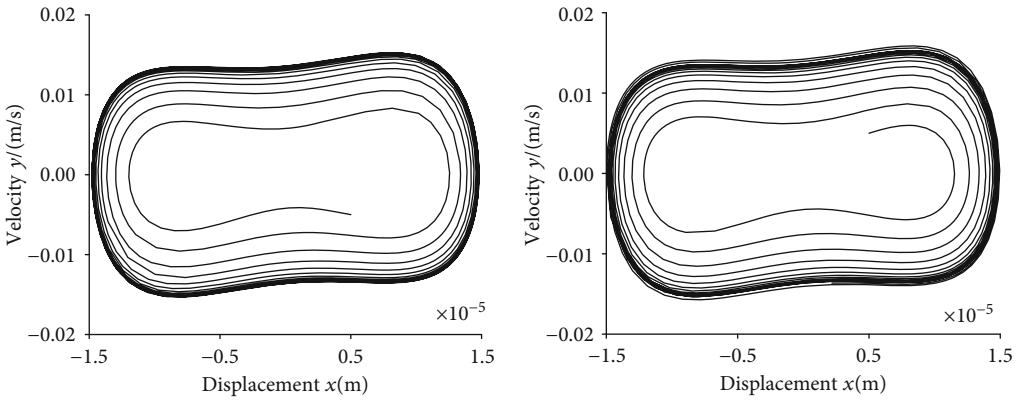

(a) ($x_0 = 0.5 \times 10^{-5}$, $v_0 = -0.005$) (b) ($x_0 = 0.5 \times 10^{-5}$, $v_0 = 0.005$)

Figure 21: Phase trajectories under $i_0 = 1.6$ A, $q_0 = 1.0 \times 10^{-4}$ m^3/s.

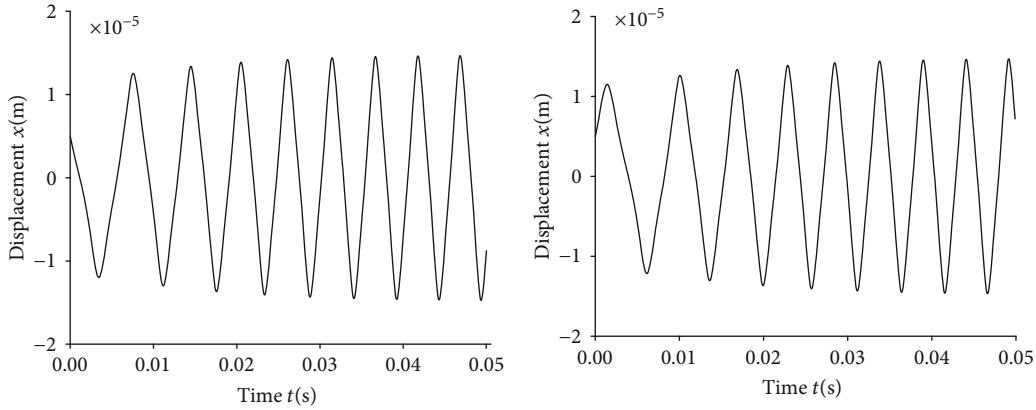

(a) ($x_0 = 0.5 \times 10^{-5}$, $v_0 = -0.005$) (b) ($x_0 = 0.5 \times 10^{-5}$, $v_0 = 0.005$)

FIGURE 22: $x - t$ curves under $i_0 = 1.6$ A, $q_0 = 1.0 \times 10^{-4}$ m^3/s.

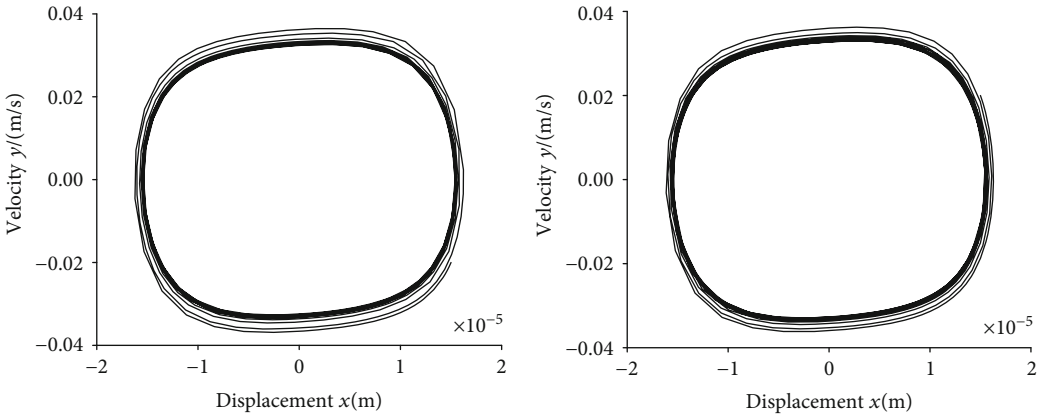

(a) ($x_0 = 1.5 \times 10^{-5}$, $v_0 = -0.02$) (b) ($x_0 = 1.5 \times 10^{-5}$, $v_0 = 0.02$)

FIGURE 23: Phase trajectories under $i_0 = 1.8$ A, $q_0 = 1.6 \times 10^{-4}$ m^3/s.

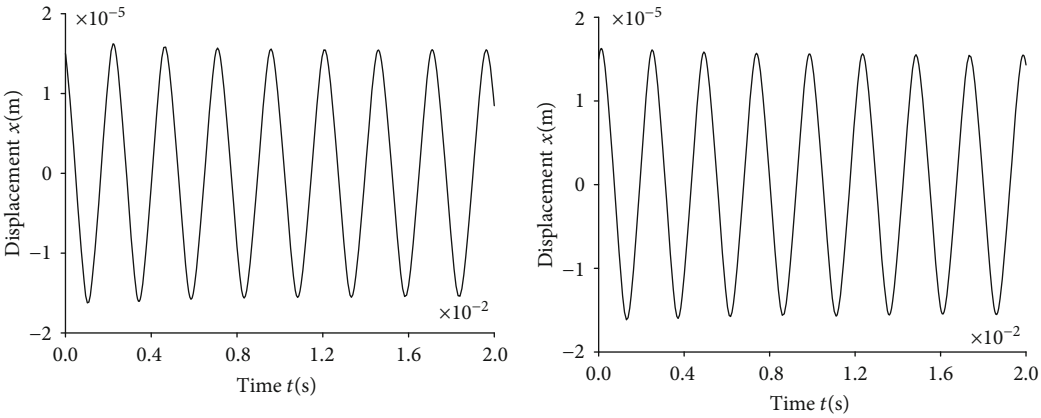

(a) ($x_0 = 1.5 \times 10^{-5}$, $v_0 = -0.02$) (b) ($x_0 = 1.5 \times 10^{-5}$, $v_0 = 0.02$)

FIGURE 24: $x - t$ curves under $i_0 = 1.8$ A, $q_0 = 1.6 \times 10^{-4}$ m^3/s.

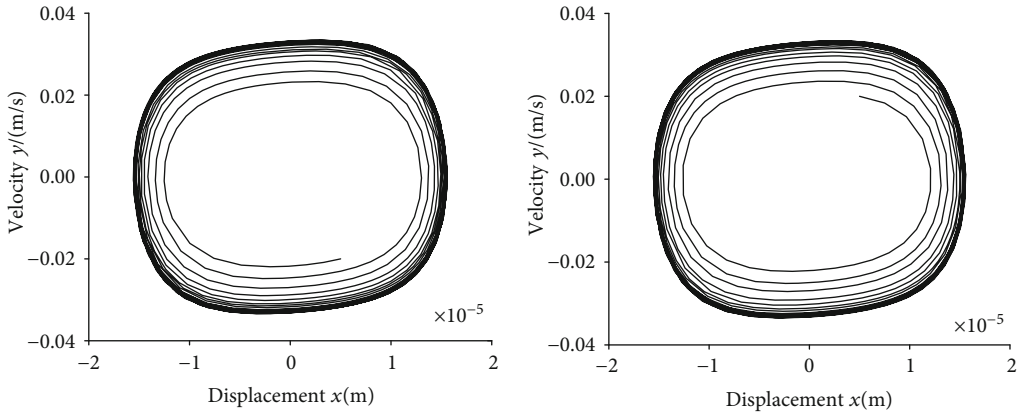

(a) ($x_0 = 0.5 \times 10^{-5}$, $v_0 = -0.02$) (b) ($x_0 = 0.5 \times 10^{-5}$, $v_0 = 0.02$)

FIGURE 25: Phase trajectories under $i_0 = 1.8$ A, $q_0 = 1.6 \times 10^{-4}$ m^3/s.

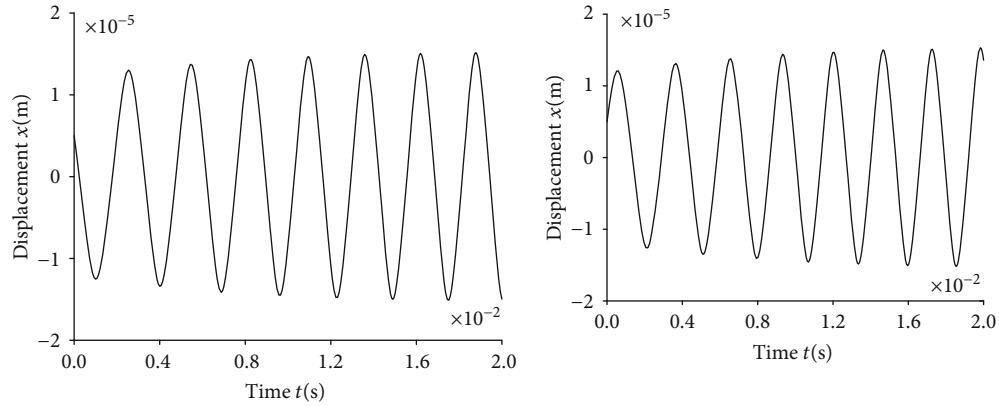

(a) ($x_0 = 0.5 \times 10^{-5}$, $v_0 = -0.02$) (b) ($x_0 = 0.5 \times 10^{-5}$, $v_0 = 0.02$)

FIGURE 26: $x - t$ curves under $i_0 = 1.8$ A, $q_0 = 1.6 \times 10^{-4}$ m^3/s.

The phase trajectories of initial point (1.5×10^{-5}, -0.02) and (1.5×10^{-5}, 0.02) both surround and approach the stable focus (0, 0). Both of them reach balance after 0.05 s adjustment, and the rotor can be suspended stably as shown in Figures 15 and 16. The balance position is the expected center of rotation, and the phase trajectories of different initial points eventually approach the same stable focus.

(3) Assume that $i_0 = 1.6$ A, $q_0 = 0.25 \times 10^{-4}$ m^3/s, and phase trajectories and $x - t$ curves are shown in Figures 17 and 18

The phase trajectory of point (-1.5×10^{-5}, 0.02) rapidly approaches stable focus (0.76×10^{-5}, 0), while the phase trajectory of point (2.63×10^{-5}, 0) gradually surrounds and approaches stable focus (2.63×10^{-5}, 0). Both of them reach balance after 0.0012 s adjustment, and the rotor can be suspended stably as shown in Figures 17 and 18. However, the balance position is not the expected center of rotation, and the phase trajectories of different initial points eventually approach different stable focus.

(4) Assume that $i_0 = 1.8$ A, $q_0 = 1.2 \times 10^{-4}$ m^3/s, and phase trajectories and $x - t$ curves are shown in Figures 19 and 20

According to Figures 19 and 20, the rotor oscillates in equal amplitude, and the phase trajectories form a limit cycle.

In order to verify the stability of the limit cycle, the initial point inside the limit cycle was selected to simulate the phase trajectories and $x - t$ curves as shown in Figures 21 and 22.

According to Figures 21 and 22, the phase trajectories of the inner initial point gradually diverge and finally approach a limit cycle, so the rotor cannot be suspended stably in this case [18].

(5) Assume that $i_0 = 1.8$ A, $q_0 = 1.6 \times 10^{-4}$ m^3/s, and phase trajectories and $x - t$ curves are shown in Figures 23 and 24

According to Figures 23 and 24, the rotor oscillates in equal amplitude, and phase trajectories form a limit cycle [19].

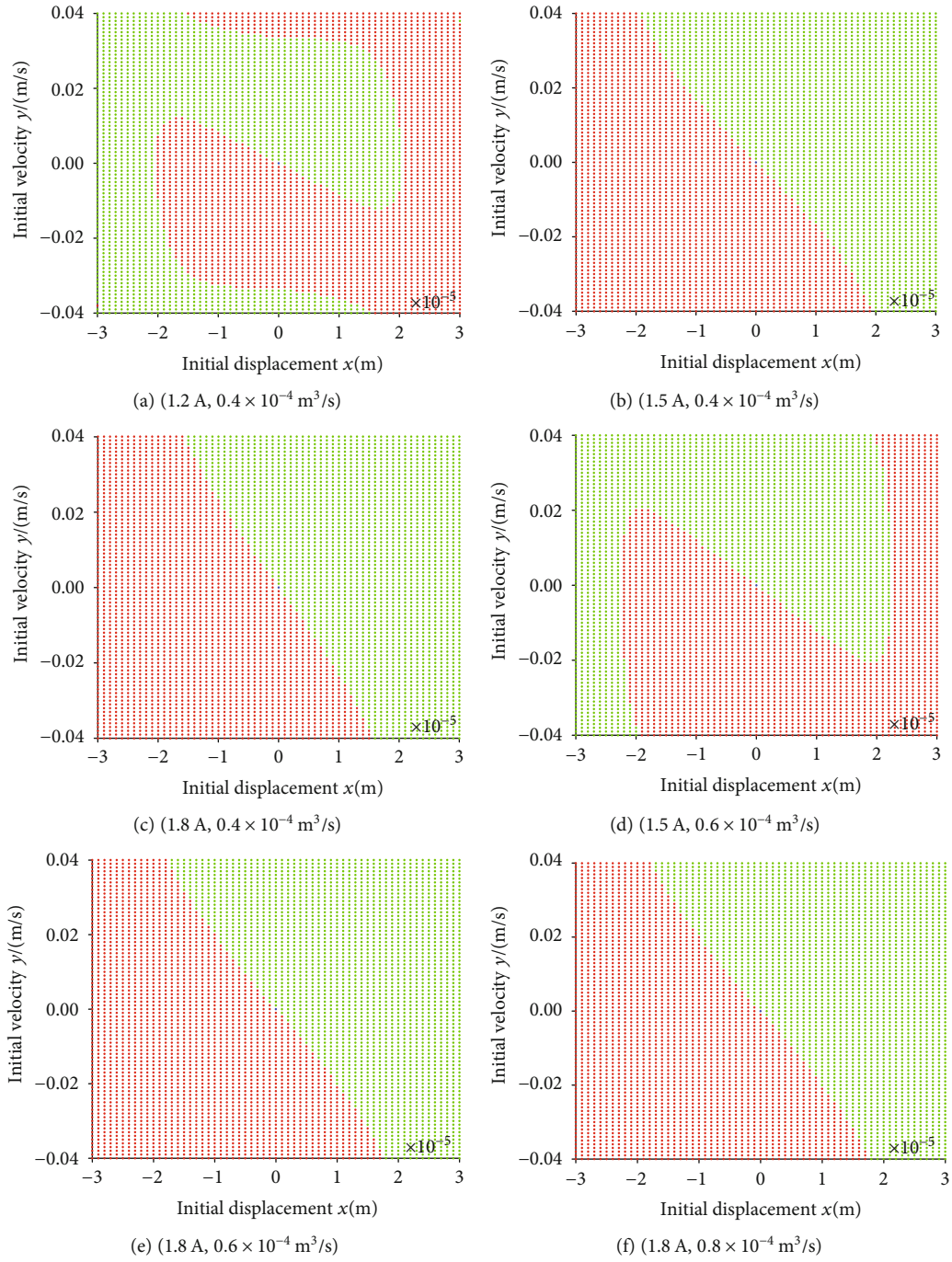

Figure 27: Basins of attraction under different parameters.

In order to verify the stability of the limit cycle, the initial point inside the limit cycle was selected to simulate the phase trajectories and $x-t$ curves as shown in Figures 25 and 26.

According to Figures 25 and 26, the phase trajectories of inner initial points gradually diverge and finally approach a limit cycle, so the rotor cannot be suspended stably in this case.

With the gradual change of i_0 and q_0, different initial positions of the rotor are attracted to different stable singularities. Basins of attraction under different parameter groups are shown in Figure 27. The red and green areas are, respectively, attracted to singularity $(x_{2,1}, 0)$ and $(x_{2,2}, 0)$.

According to Figure 27, singularity positions to which rotor is eventually attracted depend not only on initial velocity and initial displacement but also on coil current i_0 and flow of bearing cavity q_0. When i_0 is small, the attraction of singularities will change greatly with i_0 change slightly. When q_0 is large, the attraction of singularities will change greatly with q_0 change slightly.

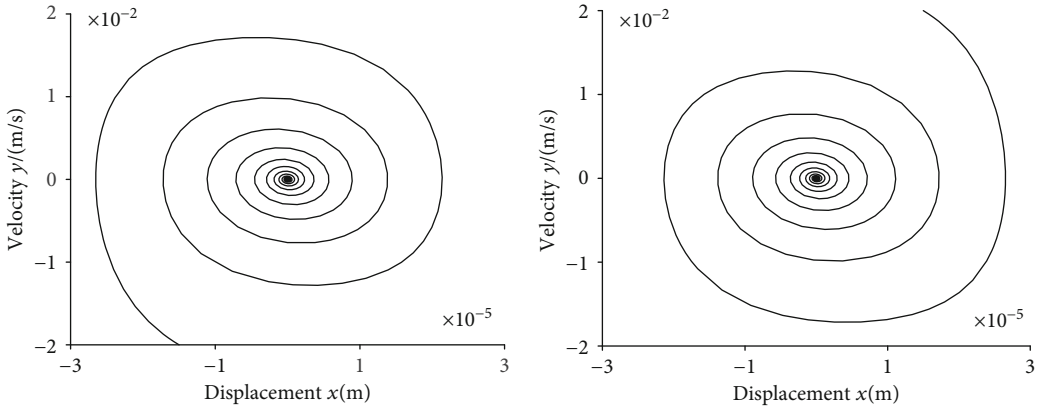

(a) $(-1.50 \times 10^{-5}, -0.02)$ (b) $(1.50 \times 10^{-5}, 0.02)$

FIGURE 28: Phase trajectories under $h_0 = 5.0 \times 10^{-5}$ m, $l = 5.0 \times 10^{-5}$ m.

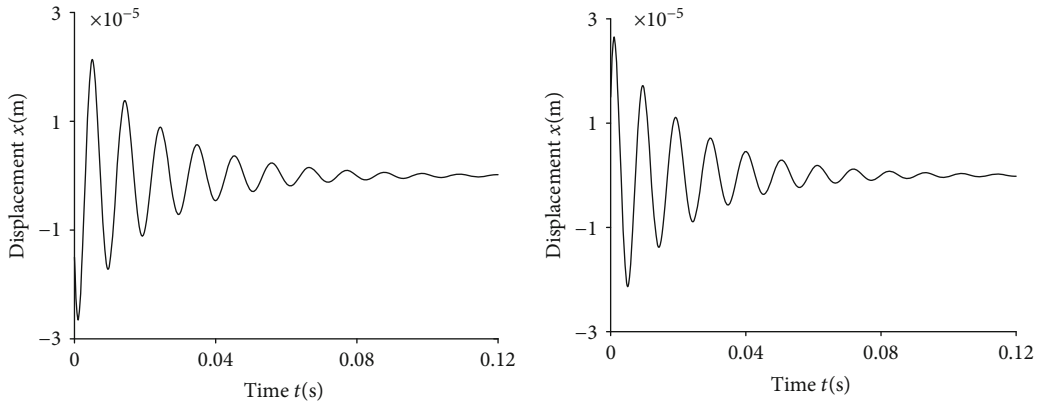

(a) $(-1.50 \times 10^{-5}, -0.02)$ (b) $(1.50 \times 10^{-5}, 0.02)$

FIGURE 29: $x - t$ curves under $h_0 = 5.0 \times 10^{-5}$ m, $l = 5.0 \times 10^{-5}$ m.

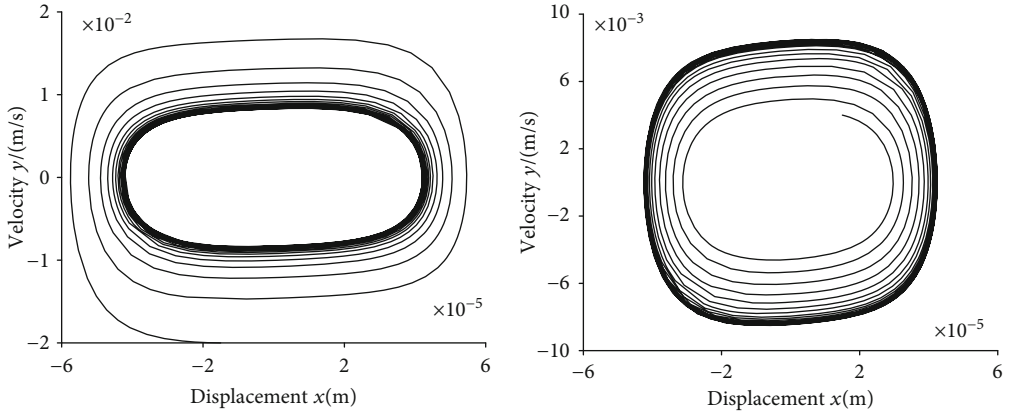

(a) $(-1.50 \times 10^{-5}, -0.02)$ (b) $(1.50 \times 10^{-5}, 4.00 \times 10^{-3})$

FIGURE 30: Phase trajectories under $h_0 = 8.0 \times 10^{-5}$ m, $l = 2.0 \times 10^{-5}$ m.

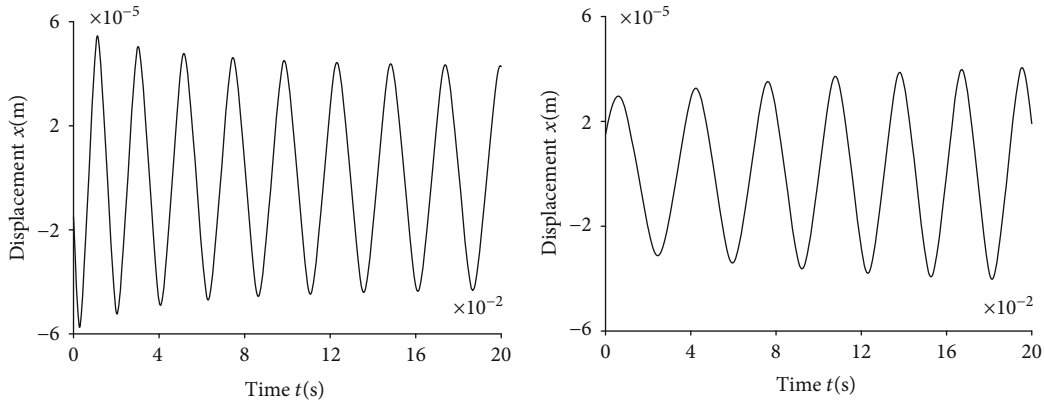

(a) $(-1.50 \times 10^{-5}, -0.02)$ (b) $(1.50 \times 10^{-5}, 4.00 \times 10^{-3})$

FIGURE 31: $x - t$ curves under $h_0 = 8.0 \times 10^{-5}$ m, $l = 2.0 \times 10^{-5}$ m.

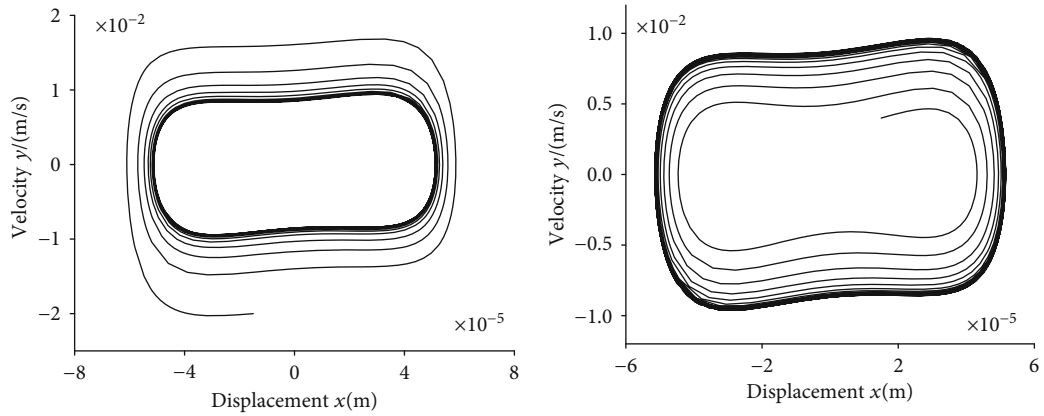

(a) $(-1.50 \times 10^{-5}, -0.02)$ (b) $(1.50 \times 10^{-5}, 4.00 \times 10^{-3})$

FIGURE 32: Phase trajectories under $h_0 = 8.0 \times 10^{-5}$ m, $l = 1.0 \times 10^{-5}$ m.

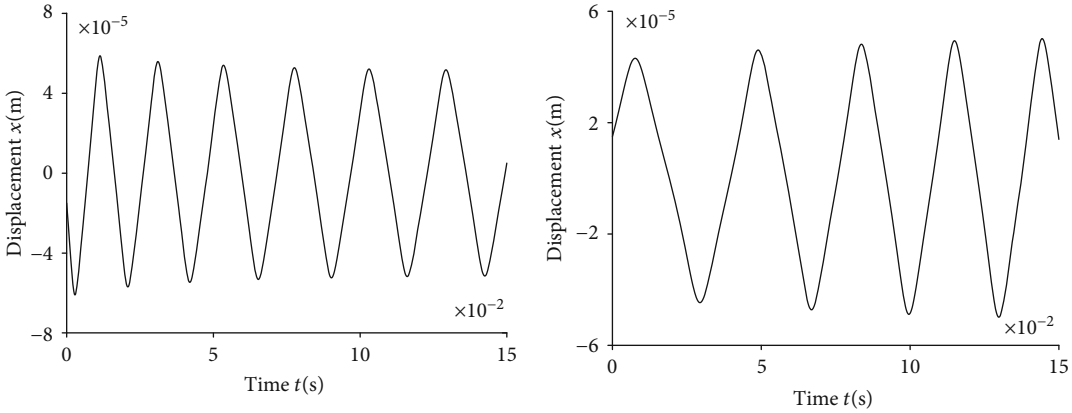

(a) $(-1.50 \times 10^{-5}, -0.02)$ (b) $(1.50 \times 10^{-5}, 4.00 \times 10^{-3})$

FIGURE 33: $x - t$ curves under $h_0 = 8.0 \times 10^{-5}$ m, $l = 1.0 \times 10^{-5}$ m.

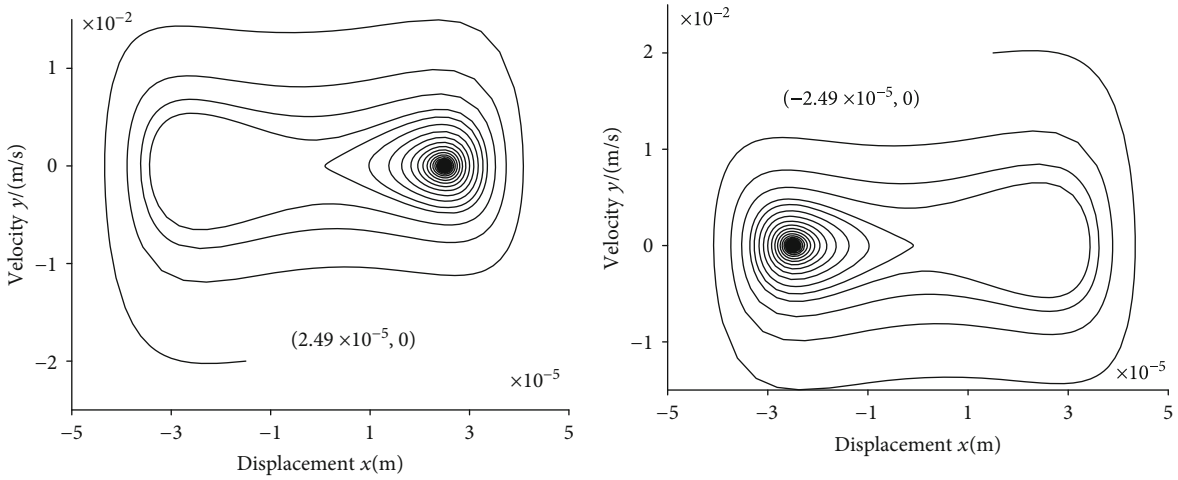

(a) $(-1.50 \times 10^{-5}, -0.02)$ (b) $(1.50 \times 10^{-5}, 0.02)$

FIGURE 34: Phase trajectories under $h_0 = 6.0 \times 10^{-5}$ m, $l = 0.5 \times 10^{-5}$ m.

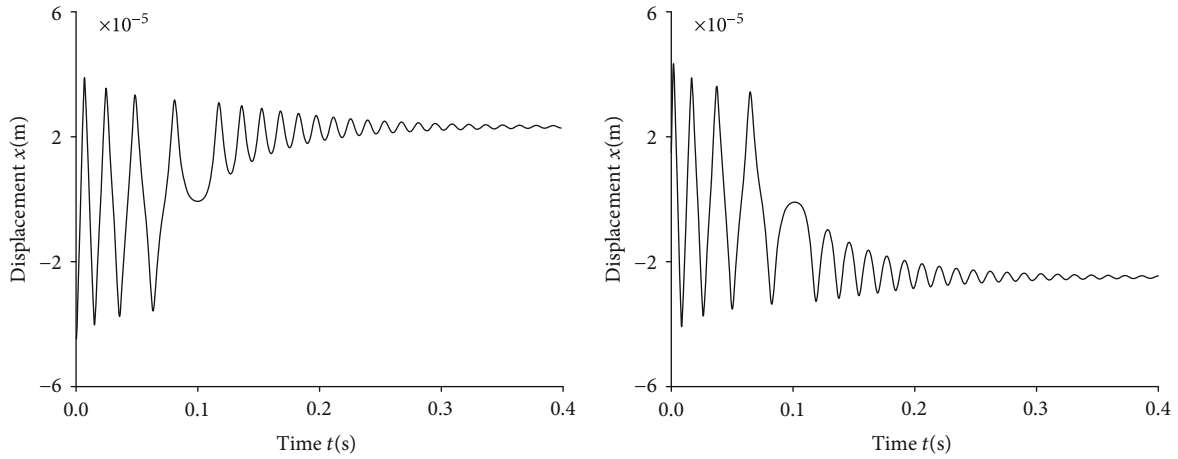

(a) $(-1.50 \times 10^{-5}, -0.02)$ (b) $(1.50 \times 10^{-5}, 0.02)$

FIGURE 35: $x - t$ curves under $h_0 = 6.0 \times 10^{-5}$ m, $l = 0.5 \times 10^{-5}$ m.

4.2. Phase Trajectories and Attractively under Parameter Group (h_0, l)

(1) Assume that $h_0 = 5.0 \times 10^{-5}$ m, $l = 5.0 \times 10^{-5}$ m, and the phase trajectories and $x - t$ curves are shown in Figures 28 and 29

According to Figures 28 and 29, the phase trajectories of initial point $(-1.5 \times 10^{-5}, -0.02)$ and $(1.5 \times 10^{-5}, 0.02)$ both surround and gradually approach the stable focus (0, 0). Both of them reach balance after 0.12 s adjustment, and the rotor can be suspended stably. And the balance position is the expected center of rotation [20].

(2) Assume that $h_0 = 8.0 \times 10^{-5}$ m, $l = 2.0 \times 10^{-5}$ m, and the phase trajectories and $x - t$ curves are shown in Figures 30 and 31

According to Figures 30 and 31, the phase trajectories of initial point $(-1.5 \times 10^{-5}, -0.02)$ and $(1.5 \times 10^{-5}, 0.004)$, respectively, surround and gradually approach different limit cycles after multiple periodic adjustments. There is no stable singularity. The rotor cannot be suspended stably, and Hopf bifurcation may occur in the system [21].

(3) Assume that $h_0 = 8.0 \times 10^{-5}$ m, $l = 1.0 \times 10^{-5}$ m, and the phase trajectories and $x - t$ curves are shown in Figures 32 and 33

According to Figures 32 and 33, the phase trajectories of initial point $(-1.5 \times 10^{-5}, -0.02)$ and $(1.5 \times 10^{-5}, 0.004)$, respectively, surround and gradually approach different limit cycles after multiple periodic adjustments. There is no stable singularity. The rotor cannot be suspended stably, and Hopf bifurcation may occur in the system [22].

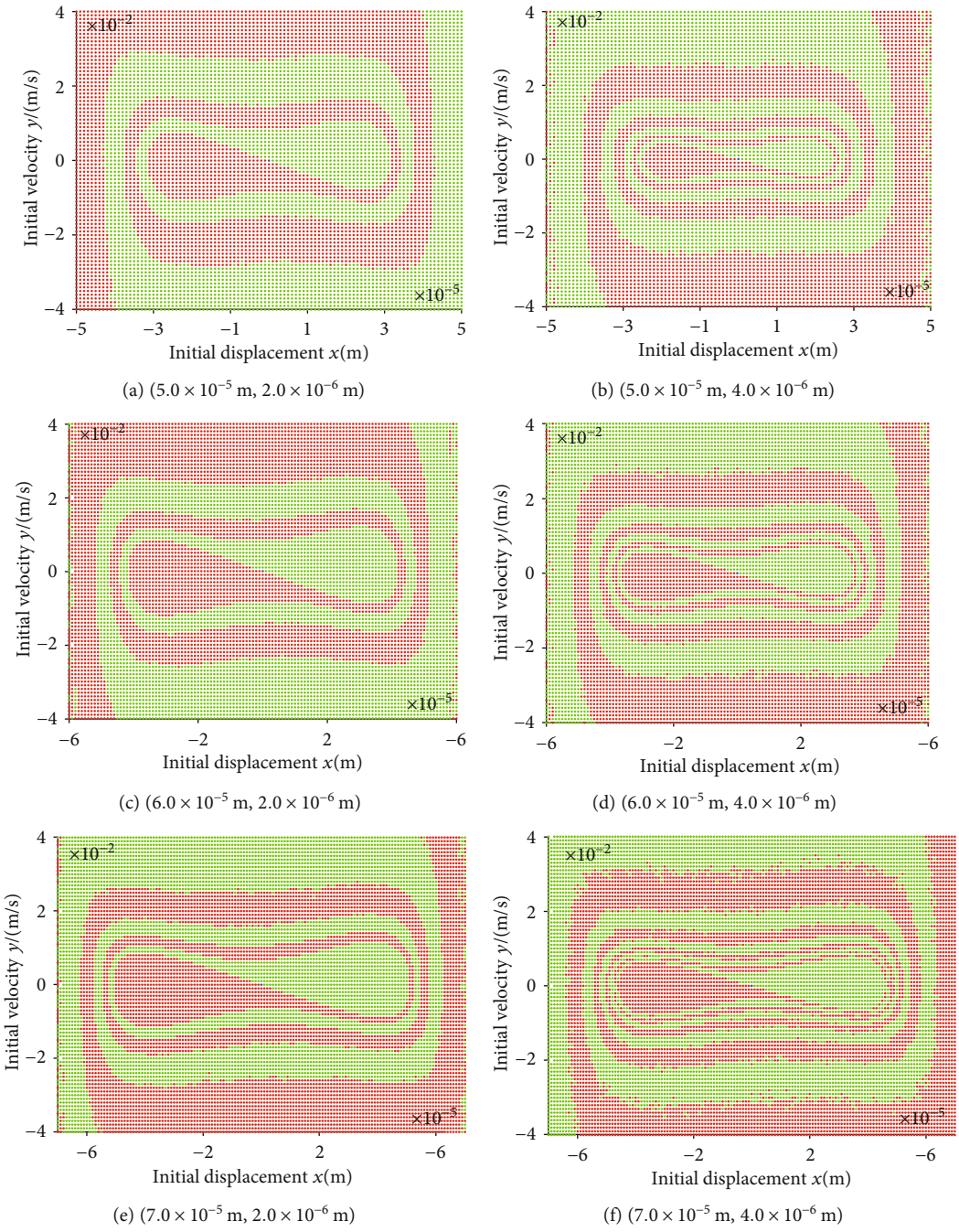

Figure 36: Basin of attraction under different parameters.

(4) Assume that $h_0 = 8.0 \times 10^{-5}$ m and $l = 1.0 \times 10^{-5}$ m, and the phase trajectories and $x - t$ curves are shown in Figures 34 and 35

According to Figures 34 and 35, the phase trajectory of initial phase point $(-1.50 \times 10^{-5}, -0.02)$ gradually approaches stable focus $(2.49 \times 10^{-5}, 0)$, while initial phase point $(1.50 \times 10^{-5}, 0.02)$ gradually approaches stable focus $(-2.49 \times 10^{-5}, 0)$. Both of them reach balance after 0.4 s adjustment, and the rotor can be suspended stably. However, the balance position is not the expected center of rotation [23].

To sum up, the final balance position is affected not only by the initial phase point but also by oil film thickness h_0 and galvanized layer thickness l. And final balance position of the same initial phase point will be different under the combined influence of different h_0 and l. Therefore, it is necessary to simulate basins of attraction under different h_0 and l conditions.

With the change of h_0 and l, the characteristics of the basin of attraction will be changed as well. Basins of attraction under different parameters are shown in Figure 36.

According to Figure 36, the basins of attraction are distributed symmetrically. The phase points in the red region will be eventually attracted to the nonzero singularity $(x_{2,1}, 0)$, while the green region is attracted to singularity $(x_{2,2}, 0)$ [24]. Moreover, the final stable balance position of the rotor changes greatly with l change slightly, while the final equilibrium point is slightly affected by h_0.

5. Conclusion

The paper presents the static bifurcation behavior of MLDSB affected by design parameters. The singularity characteristics, phase trajectory, $x - t$ curves, and suction basin of the single DOF bearing system are analyzed to verify the accuracy of the theoretical calculation. The conclusions are as follows.

(1) Nonzero singularities exist and static bifurcation occurs when $\varepsilon_2 > 0$ or $\delta_2 > 0$

(2) With flow of bearing cavity, coil current, oil film thickness, and galvanized layer thickness changes, in turn, the singularities will convert between stable focus, unstable focus, stable node, and saddle point

(3) As current i_0, flow q_0, oil film thickness h_0, and zinc layer thickness l change, the phase trajectory may form a stability limit cycle, and the system oscillates at constant amplitude, which makes it impossible to achieve stable suspension

(4) The attractiveness of singularity will change greatly when the flow of bearing cavity and coil current change slightly in the case of small current or large flow

(5) The minimal change of galvanized layer thickness will lead to the fundamental change of the final stable equilibrium point of the rotor, while the final equilibrium point is less affected by the oil film thickness

Data Availability

The [DATA TYPE] data used to support the findings of this study are included within the article.

Conflicts of Interest

The authors declare that they have no conflicts of interest.

References

[1] J. Zhao, W. Yan, Z. Wang, D. Gao, and G. Du, "Study on clearance-rubbing dynamic behavior of 2-DOF supporting system of magnetic-liquid double suspension bearing," *Processes*, vol. 8, no. 8, pp. 973–988, 2020.

[2] H. Yu, Y. S. Chen, and Q. J. Cao, "Nonlinear dynamic behavior analysis for a cracked multi-DOF rotor system," *Journal of Vibration and Shock*, vol. 7, pp. 92–98, 2014.

[3] J. H. Zhao, G. J. Zhang, D. R. Gao, and G. J. Du, "Decoupling control of single DOF supporting system of magnetic-liquid double suspension bearing," *Machine Tool and Hydraulics*, vol. 48, no. 18, pp. 1–8, 2020.

[4] Z. Y. Xie, W. X. Mou, H. K. Zhou, and X. Wang, "Variable parameter control of active magnetic bearing rotor system based on rotation speed," *Journal of Vibration Engineering*, vol. 25, no. 6, pp. 739–744, 2012.

[5] K. Wang, X. Y. Li, L. J. Zhang, and H. B. Zhang, "Dynamical simulations of a bistable piezoelectric energy harvesting system with elastic support," *Hebei University of Science and Technology*, vol. 40, no. 3, pp. 242–251, 2019.

[6] Q. Hai and S. T. Liu, "Spatial static bifurcation of 2-D discrete dynamical systems and its control," *Scientia Sinica Informationis*, vol. 47, no. 3, pp. 351–361, 2016.

[7] J. M. Pu Y. D. Hu et al., "Principal resonance bifurcation and chaos of rotating annular plates in magnetic fields," *Applied Mathematics and Mechanics*, vol. 37, no. 11, pp. 1181–1197, 2016.

[8] H. Y. Luo, Y. F. Wang, and C. W. Wu, "Nonlinear vibration and bifurcation of continuous rotor bearing systems excited by electromagnetic force," *Chinese Journal of Applied Mechanics*, no. 6, pp. 624–628, 2011.

[9] X. Zhao and Y. H. Li, "The bifurcation problem of a kind of pendulum physical model," *Journal of Beijing University*, no. 4, pp. 653–657, 2016.

[10] R. R. Peng, "Research on nonlinear vibration characteristics of parametrically excited stiffness of 2-DOF rolling," *Steel Rolling*, vol. 32, no. 6, pp. 40–47, 2015.

[11] J. H. Zhao, T. Chen, Q. Wang, B. Zhang, and D. R. Gao, "Stability analysis of single DOF support system of magnetic-liquid double suspension bearing," *Machine Tool and Hydraulics*, vol. 47, no. 6, pp. 1–7, 2019.

[12] Y. Wu, Y. J. Lu, and K. Luo, "Motion stability of the rotor system supported by electromagnetic bearings," *Journal of Xi'an Shiyou University*, vol. 21, no. 4, pp. 94–97, 2006.

[13] G. Zhang, Q. Z. Yin, and S. P. Liang, "Research on nonlinear dynamics of five-DOF active magnetic bearings-rotor system," *Journal of Mechanical Engineering*, vol. 46, no. 20, pp. 15–21, 2010.

[14] X. Shan, "Dynamic behavior analysis of magnetic levitation rotor system," *Era Agricultural Machinery*, vol. 42, no. 12, pp. 34–36, 2015.

[15] B. Gerislioglu, A. Ahmadivand, M. Karabiyik, R. Sinha, and N. Pala, "VO2-based reconfigurable antenna platform with addressable microheater matrix," *Advanced Electronic Materials*, vol. 3, no. 9, article 1700170, 2017.

[16] H. Hoshi, T. Shinshi, and S. Takatani, "Third-generation blood pumps with mechanical noncontact magnetic bearings," *Artificial Organs*, vol. 30, no. 5, pp. 324–338, 2006.

[17] S. Bulgarevich, M. Boiko, and K. Lebedinskii, "Adsorption separation of components of liquid lubricant on rubbing surfaces under sliding friction," *Journal of Friction and Wear*, vol. 36, no. 6, pp. 534–541, 2015.

[18] Y. Shang, J. Lin, X. Liu, and X. Xin, "Impact of hydrostatic bearings on the dynamic performance of electric spindle rotor device," *Mechanical Science and Technology for Aerospace Engineering*, vol. 34, no. 5, pp. 688–693, 2015.

[19] X. H. Zhou and D. L. Wang, "Bifurcation and chaos of rolling bearing system with loose rotor," *Guangdong Chemical Industry*, vol. 36, no. 11, pp. 170–172, 2009.

[20] B. Gerislioglu, L. Dong, A. Ahmadivand, H. Hu, P. Nordlander, and N. J. Halas, "Monolithic metal dimer-on-

film structure: new plasmonic properties introduced by the underlying metal," *Nano Letters*, vol. 20, no. 3, pp. 2087–2093, 2020.

[21] S. H. Gao, X. H. Yong, and G. Meng, "Three bifurcation forms of spindle rolling bearing system," *Vibration and Shock*, vol. 4, pp. 59–64, 2009.

[22] J. Feng, Y. Jinfu, and Y. Xiaoyang, "Hopf bifurcation and stability analysis of flexible rotor-bearing system," *Journal of Vibration Engineering*, vol. 14, no. 2, pp. 723–732, 2012.

[23] L. Cui, C. L. Liu, and J. R. Zheng, "Bifurcation of periodic motion of rigid rotor system with cylindrical roller bearings," *Vibration, Testing and Diagnosis*, vol. 5, pp. 637–641, 2011.

[24] Y. Sekiguchi, N. Nakagawa, H. Yoshida, and N. Saruwatari, "Chaos analysis and diagnosis of ball bearing vibration," *Journal of Japan Society for Design Engineering*, vol. 39, pp. 100–107, 2004.